

Chapter 2

The escape probability approach to opacity

It is clear that opacity as a phenomenon is at its most challenging in plasmas that exist between the two extreme regimes of thermodynamic equilibrium (eg. the photosphere) and optically thin plasma (eg. the corona). Between the photosphere and the corona the electron density varies from $\sim 10^{14}$ to $\sim 10^9$ cm^{-3} (see fig. 1.7) and conditions change from those of thermodynamic equilibrium to optically thin so that in between – i.e. in the chromospheric and the TR – there exists non-LTE plasma of significant opacity. Conditions and emission from such plasmas are complicated by long range coupling due to photo-absorption that may involve different electronic transitions and potentially a variety of atomic species. Consequently, a bound electron in a plasma, will potentially ‘see’ the rest of the plasma to some considerable distance or even in its entirety and conditions at this point are thus determined by those at all ‘visible’ positions. Each point in an optically thick plasma is therefore coupled in terms of energy and excitation to non-local regions with potentially different temperatures, densities, geometries and flows.

Opacity modifies the excited state population structure of an ion via the introduction of photo-excitation terms in the statistical balance equations. In turn, this modification influences spectral line emission. Additionally, the emission along a line-of-sight is affected by opacity due to a loss of photons along that line-of-sight either

by absorption or scattering. It follows that opacity influences radiative cooling (or heating) timescales which are relevant to radiative power loss. Even though the local radiative power loss coefficients in a dynamic plasma may not be sensitive to opacity, the time taken for photons to propagate through and escape from an emitting structure is sensitive. Therefore opacity must be significant from an energy transport perspective in at least some dynamic plasmas. Furthermore, photoionisation will alter the ionisation balance which in turn modifies spectral emission characteristics and the radiative power loss functions at a particular temperature.

A more subtle effect is that of partial frequency redistribution which relates to the ultimate fate of absorbed photons. The effect of this is to diffuse photons in frequency space toward the line wings thus altering (principally but not exclusively) emergent line profiles.

The emission from an optically thick plasma is characterised by two sets of coupled differential equations, namely those of radiative transfer and statistical balance – eqs 2.1 and 2.2 respectively.

$$\frac{dI_\nu(s)}{ds} = j_\nu(s) - \kappa_\nu(s)I_\nu(s) \quad (2.1)$$

$$\begin{aligned} \frac{dN_u(\mathbf{r})}{dt} &= -A_{u \rightarrow l}N_u(\mathbf{r}) + \frac{4\pi}{c}B_{l \rightarrow u}N_l(\mathbf{r}) \int \bar{I}_\nu(\mathbf{r})\phi(\nu)d\nu \\ &+ \textit{other collisional and radiative terms} \end{aligned} \quad (2.2)$$

These were discussed in some detail in secs. 1.2 and 1.3. Eq. 2.2 is written here for level u and differs from eq. 1.5 in that the photo-absorption process corresponding to the transition $l \rightarrow u$ has been included and the spatial dependence is made explicit. Statistical balance holds if all derivatives, $dN_u(\mathbf{r})/dt$, are zero. That is, it holds for ions whose atomic populations are in steady state. If this is so then the loss of electrons from a level due to excitation, de-excitation, ionisation and recombination is balanced, statistically speaking, by the reverse processes that serve to populate the level. This contrasts with thermodynamic equilibrium where each process is balanced by its inverse (detailed balance).

The radiative transfer equations describe the propagation of photons along a line-of-sight and so have obvious relevance to observed emission. In integrating eq. 2.1,

contributions to the intensity, both negative and positive, at each point, are summed. Coupling with eq. 2.2 is via the dependence on the population distribution terms implicit within the emission and the absorption coefficients which are proportional to the upper and lower level populations respectively. Coupling also acts in the reverse direction since the statistical balance equations require for their solution at any particular point, knowledge of the radiation field. This term involves an integration of the intensity along every line-of-sight that terminates at the point of interest and thus requires, in principle, the solution of eq. 2.1 along each of these lines of sight.

It is then clear that opacity presents a significant difficulty and, as discussed in sec. 1.3.2, a number of approaches exist to deal with it. In this work spectral emission in lines of moderate opacity is of interest with the focus being on emitting plasma structure. For such lines the relative simplicity of the escape probability approach is desirable since it allows complex emitting geometries to be considered. In this chapter the escape probability and associated quantities will be defined and evaluated and applied to data from the SOHO-SUMER spectrometer to extract optical depths of spectral lines of C II and C III. Escape probabilities will also be used in conjunction with some simple stratified atmosphere models to determine their effectiveness in describing the observed spectral emission characteristics on crossing the solar limb. In subsequent chapters the escape probability and absorption factor expressions will be analysed and developed for use within more detailed atmosphere models.

2.1 The effect of opacity on emergent intensities

The escape probability approach fits naturally within a collisional radiative framework allowing opacity to be included in the equations of statistical balance. The following definitions are made:

1. intensity, I_ν – the number of photons of frequency ν propagating in a given direction, crossing a unit area perpendicular to that direction, per unit volume, per unit time, per unit solid angle, with units $\text{cm}^{-2}\text{s}^{-1}\text{sr}^{-1}$.
2. emissivity, j_ν – the number of photons of frequency ν emitted at a point per

unit volume, per unit time, per unit solid angle, with units $\text{cm}^{-3}\text{s}^{-1}\text{st}^{-1}$.

3. absorption coefficient, κ_ν – defined such that $\kappa_\nu I_\nu$ is the number of photons of frequency ν absorbed at a point per unit volume, per unit time per unit solid angle. κ_ν has units of cm^{-1} .

These definitions lead to the following:

$$j_\nu(\mathbf{r}) = \frac{1}{4\pi} A_{u \rightarrow l} N_u(\mathbf{r}) \phi_e(\nu) \quad (2.3)$$

$$\kappa_\nu(\mathbf{r}) = \frac{1}{c} N_l h \nu B_{l \rightarrow u} \phi_a(\nu) \quad (2.4)$$

where $\phi_e(\nu)$ and $\phi_a(\nu)$ are the emission and absorption profiles respectively. From these, eqs 2.1 and 2.2 may be rewritten as follows

$$\frac{dI(s)}{ds} = \frac{1}{4\pi} A_{u \rightarrow l} N_u(s) \left[1 - \frac{N_l(s) \omega_u}{N_u(s) \omega_l} \frac{c^2}{2\nu_0^2} \int I_\nu(s) \phi_e(\nu) d\nu \right] \quad (2.5)$$

$$\begin{aligned} \frac{dN_u(\mathbf{r})}{dt} &= -A_{u \rightarrow l} N_u(\mathbf{r}) \left[1 - \frac{N_l(\mathbf{r}) \omega_u}{N_u(\mathbf{r}) \omega_l} \frac{c^2}{2\nu_0^2} \int \bar{I}_\nu(\mathbf{r}) \phi_a(\nu) d\nu \right] \\ &+ \text{ other collisional and radiative terms} \end{aligned} \quad (2.6)$$

Here ds is an element of distance along the line of sight, $A_{u \rightarrow l}$ is the Einstein A-coefficient, N_u and N_l are the upper and lower level population densities respectively and the ω 's are statistical weights.

The terms in the brackets are markedly similar, the only difference being in the specification of the intensity terms. In the eq. 2.5 the intensity term $I_\nu(s)$ is the intensity at the point s along the path $0 \rightarrow s$ and so is related to the emissivity, $j_\nu(s)$, along that path. In eq. 2.6, however, $\bar{I}_\nu(\mathbf{r})$ is the radiation field at \mathbf{r} due to surrounding plasma and so is related to the integral of $j_\nu(\mathbf{x})$, and thus also of $N_u(\mathbf{x})$ over all points \mathbf{x} .

The escape probability approach may be illustrated if eqs 2.5 and 2.6 are re-written as follows:

$$\frac{dI(s)}{ds} = \frac{1}{4\pi} A_{u \rightarrow l} N_u(s) g(s) \quad (2.7)$$

$$\frac{dN_u(\mathbf{r})}{dt} = -A_{u \rightarrow l} N_u(\mathbf{r}) \Lambda(\mathbf{r}) + \text{the other terms} \quad (2.8)$$

$g(s)$ is the *escape probability*, representing the probability that a photon emitted at a point s in the direction of the line-of-sight will escape the plasma. $\Lambda(\mathbf{r})$ is the *Biberman-Holstein coefficient* or *net-radiative bracket* (Irons, 1979) and is called here the *absorption factor*. It relates to the probability that a photo-absorption will occur at the point \mathbf{r} . Both terms may be viewed as providing parametric adjustments to the Einstein A-coefficients in the equations of radiative transfer and statistical balance. Thus, providing the A-coefficients are modified appropriately, the optically thick population structure may be obtained in an identical manner as the optically thin one. This will be discussed in more detail later.

The escape probability was first introduced by Holstein (1947) and has subsequently been considered by many authors (e.g. McWhirter, 1965; Irons, 1979; Doyle & McWhirter, 1980). Holstein's work focused on the emission point of view but McWhirter (1965) considered the population structure and since then expressions have been used and developed in both contexts. More recent are works by Kastner & Bhatia (1989), Kastner & Kastner (1990) and Kastner & Bhatia (1992). These authors have extensively developed escape probability and absorption factor expressions and used them for predicting emergent intensities and optically thick population structures. A useful aspect to the escape probability approach is in diagnosing optical depths directly from observations – a method that was established by Jordan (1967). This technique (described in more detail below) makes use of observed branching ratios of spectral lines that share a common upper level and has been used by several authors (Doyle & McWhirter, 1980; Keenan & Kingston, 1986; Brooks et al., 2000) to extract optical depths from spectral observations of solar plasmas.

In first deriving an expression for the escape probability, Holstein, rather than evaluating the bracketed term in eq. 2.5, considered the definition of $g(s)$ as a probability of escape. If one considers the propagation of a photon by a distance d along a line of sight, the radiative transfer equation is

$$\frac{dI_\nu(s)}{ds} = -\kappa_{\nu, l \rightarrow u} I_\nu(s) \quad (2.9)$$

$$\Rightarrow I_\nu(d) = I_\nu(0) e^{-\kappa_{\nu, l \rightarrow u} d} \quad (2.10)$$

Holstein defined $T(\kappa_{\nu,l \rightarrow u} s, \nu) = \exp(\kappa_{\nu,l \rightarrow u} s)$ as the *monochromatic transmission probability*. The escape probability is this quantity averaged over the emission profile, $\phi_e(\nu)$, i.e.

$$g(s) = \int \phi(\nu)_e T(\kappa_{\nu,l \rightarrow u} s, \nu) d\nu \quad (2.11)$$

$\kappa_{\nu,l \rightarrow u}$ is in general a function of space as well as frequency but if it is assumed to be constant with respect to space, and furthermore, if emission and absorption profiles are assumed to be purely Doppler broadened, i.e.

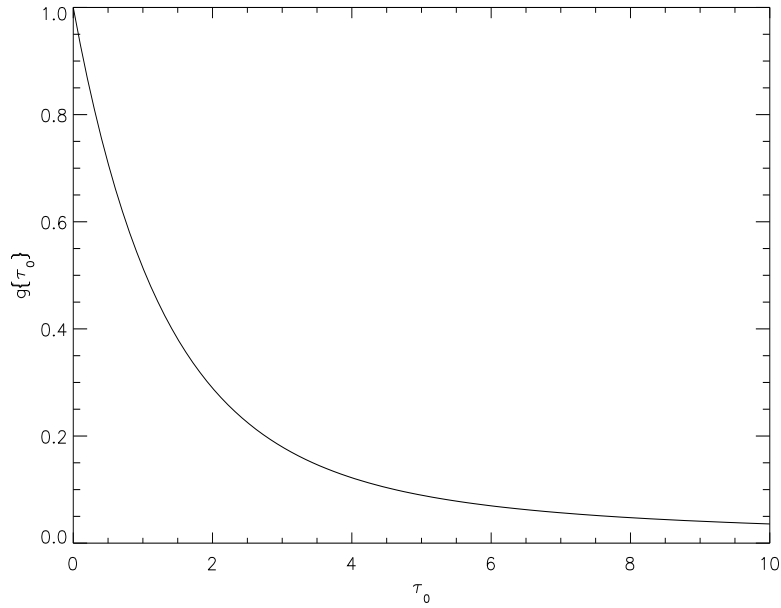


Figure 2.1: Plot of $g\{\tau_0\}$ versus τ_0 .

$$\phi_e(\nu) \equiv \phi_a(\nu) \equiv \phi(\nu) = \frac{1}{\sqrt{\pi} \Delta\nu_D} \exp\left\{-\left(\frac{\nu - \nu_0}{\Delta\nu_D}\right)^2\right\} \quad (2.12)$$

with $\Delta\nu_D$ the Doppler width, then if the line of sight is defined by $s : 0 \rightarrow L$,

$$g(s) = \frac{1}{\sqrt{\pi}} \int_{-\infty}^{\infty} e^{-u^2} \exp\{-\tau_0(s) e^{-u^2}\} du \quad (2.13)$$

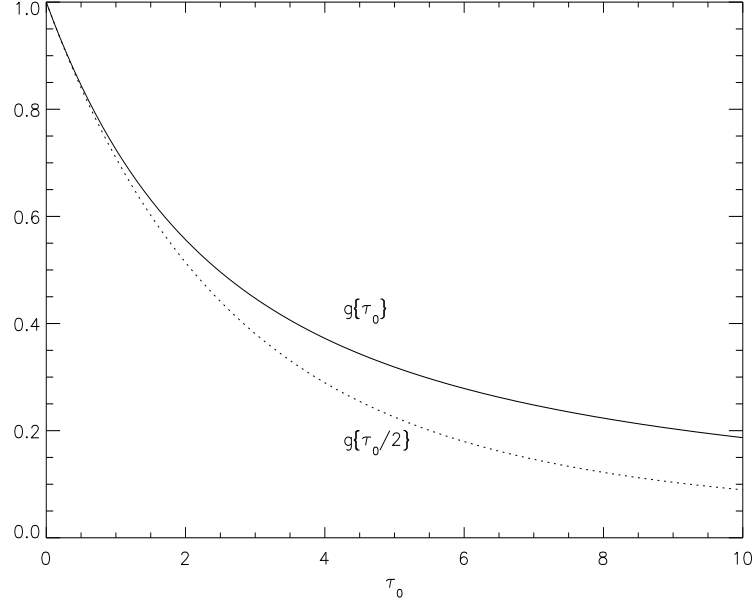


Figure 2.2: Solid line – $\bar{g}\{\tau_0\}$ versus τ_0 ; dotted line – $g\{\tau_0/2\}$ versus τ_0 (see sec. 2.6 for discussion).

where $u = (\nu - \nu_0)/\Delta\nu_D$ and $\tau_0 = \kappa_{0,l\rightarrow u}(L - s)$. It is convenient to write $g(s)$ in terms of optical depth, i.e. as $g\{\tau_0(s)\}$. Following Mitchell & Zemansky (1961),

$$\tau_0(s) = 1.16^{-6} \sqrt{M/T_i} \lambda_0 N_l f_{l\rightarrow u} (L - s) \quad (2.14)$$

where T_i is the ion temperature (K), M is the atomic mass number, λ_0 is the central wavelength (cm), N_l is the number density of the lower level of the transition (cm^{-3}), $f_{l\rightarrow u}$ is the absorption oscillator strength and L is the physical thickness of the plasma along the line of sight (cm). A plot of $g\{\tau_0\}$ versus τ_0 is shown in fig. 2.1.

Integrating eq. 2.7 yields

$$I = \frac{1}{4\pi} A_{u\rightarrow l} N_u \bar{g}\{\tau_0\} L \quad (2.15)$$

where $\bar{g}\{\tau_0\}$ is the *line-of-sight averaged escape probability* and τ_0 is the total optical depth along the line-of-sight, i.e.

$$\tau_0 = 1.16^{-6} \sqrt{M/T_i} \lambda_0 N_l f_{l\rightarrow u} L \equiv \tau_0(0) \quad (2.16)$$

Since the density is assumed constant, $\bar{g}\{\tau_0\}$ is given by

$$\bar{g}\{\tau_0\} = \frac{1}{\sqrt{\pi}} \int_{-\infty}^{\infty} \left[\frac{1 - \exp\{-\tau_0 e^{-u^2}\}}{\tau_0} \right] du \quad (2.17)$$

$\bar{g}\{\tau_0\}$ is compared to $g\{\tau_0/2\}$ in fig. 2.2.

Although $g\{\tau_0(s)\}$ is the probability of escape, it is identical to what Irons (1979) called the *transmission factor*, $T(\tau_0)$, which is a more appropriate label for a general picture. The former is a probability of escape since it relates to the likelihood of a photon propagating from its point of origin to a second point that is located *outwith* the plasma. If, however, that point is within the plasma then, though the probability is purely that of propagation from one point to another and not specifically of escape, the expression is identical. In this case *transmission factor* is the appropriate label. Kastner & Kastner (1990) describe $g\{\tau_0\}$, which they denote by $p_f(\hat{\nu}, \vec{k}, \tau : 0)$, as corresponding to the case of isolated emitters and absorbers (denoted '0') as it does not include the effect of emission at other optical depths along the line-of-sight. Averaging this expression along the line-of-sight leads to what Kastner & Kastner describe as being the *proper* escape probability for emergent intensities, given by $p_f(\hat{\nu}, \vec{k}, \tau : 1) \equiv \bar{g}\{\tau_0\}$. This represents the *mean* probability that a photon, emitted from some point along a line-of-sight of depth τ_0 , in the direction of the line-of-sight, will escape from the plasma, as described above.

This expression assumes that the only effect of opacity is to scatter photons out of the line-of-sight. This is not true as photons may also be scattered *into* the line-of-sight. This was recognised by Jordan (1967) who wrote

$$E_i \sim N_u W_i = \frac{N_u b_i q_i}{1 - \sum_n (b_n [1 - q_n])} \quad (2.18)$$

where E_i is the energy intensity ($E_i = h\nu I_i$), W_i is the fraction of photons created, escaping in line i ; q_i is equivalent in principle to $\bar{g}\{\tau_0\}$ and the denominator accounts for the scattering into the line-of-sight. This was subsequently re-written by Kastner & Bhatia (1992) as the correct line-of-sight escape probability, p_e , which is given by

$$p_{e,j} = \frac{\bar{p}_{f,j}}{1 - \sum_i b_i (1 - p_{d,i})(1 - \bar{p}_{f,i})(1 - \bar{p}_{f,i})} \quad (2.19)$$

where $p_{d,i}$ is the photon loss probability (defined as the ratio of collisional de-excitation to total de-excitation – Kastner, 1981), $\vec{p}_{f,j} = p_f(\hat{\nu}, \vec{k}, \tau : 1) \equiv \bar{g}\{\tau_0\}$, and $\bar{p}_{f,i} = p_f(\hat{\nu}, \vec{k}, \tau : 0)$. $\bar{p}_{f,i}$ is the mean probability that a photon emitted anywhere in the layer will travel to the surface and escape. This latter term is equivalent to Irons' *escape factor*, θ (Irons, 1979).

2.1.1 Deduction of opacity from observations

It was pointed out by Jordan (1967) that for intensity ratios of lines arising from a common upper level the denominator of $p_{e,j}$ cancels out leaving just $\vec{p}_{f,j} \equiv \bar{g}\{\tau_0\}$ as the appropriate escape probability for this ratio analysis.

Jordan introduced the idea that such a quantity could be used to diagnose optical depths from observations of such ratios. She wrote the energy intensity ratio of two lines, 1 and 2, arising from a common upper level as

$$\frac{E_1}{E_2} = \frac{b_1 q_1}{\lambda_1} \frac{\lambda_2}{b_2 q_2} \quad (2.20)$$

where q_1 and q_2 are the escape probabilities for lines 1 and 2 respectively (equivalent in principle to $\bar{g}\{\tau_0^{(1)}\}$ and $\bar{g}\{\tau_0^{(2)}\}$) and b_1 and b_2 are the probabilities that photons will be emitted in lines 1 and 2 respectively, i.e.

$$b_i = \frac{A_i}{\sum_n (A_n + C_n N_e) + \sum_m (u_\nu B_m + C_m N_e)} \quad (2.21)$$

where the sum over n refers to processes below the excited level and the sum over m refers to processes above the excited level. $C_n N_e$ is the collisional de-excitation rate, $C_m N_e$ is the collisional excitation rate and $u_\nu B_m$ is the photo-excitation rate. Although her escape probability expression was much simpler than those considered here and was derived by assuming that all photons emitted in the line wings where $\tau < 1$ escape whereas all those emitted near line centre where $\tau > 1$ do not, the idea is effective. In the present notation, equation 2.20 is

$$\frac{I_{u \rightarrow l_1}}{I_{u \rightarrow l_2}} = \frac{A_{u \rightarrow l_1} \bar{g}\{\tau_{0,l_1 \rightarrow u}\}}{A_{u \rightarrow l_2} \bar{g}\{\tau_{0,l_2 \rightarrow u}\}} \quad (2.22)$$

$$\Rightarrow \frac{\bar{g}\{\tau_{0,l_1 \rightarrow u}\}}{\bar{g}\{\tau_{0,l_2 \rightarrow u}\}} = \frac{I_{u \rightarrow l_1} A_{u \rightarrow l_2}}{I_{u \rightarrow l_2} A_{u \rightarrow l_1}} \quad (2.23)$$

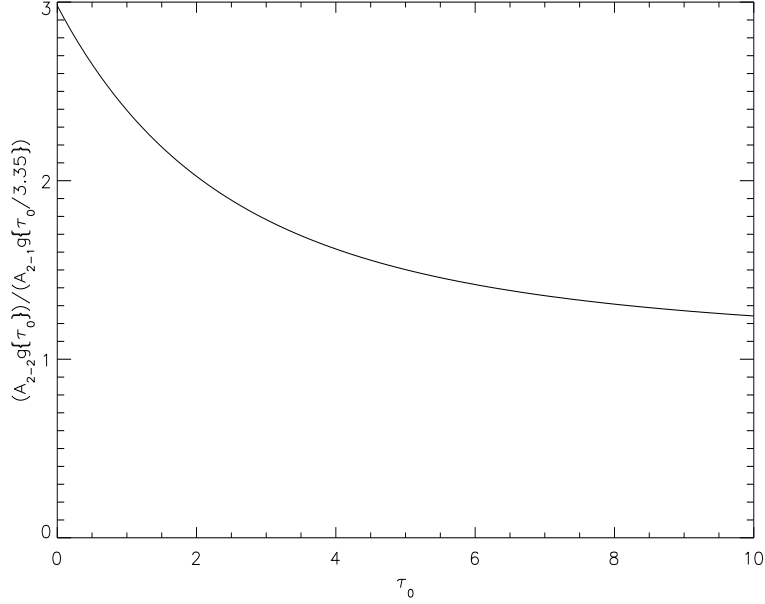


Figure 2.3: Plot of $A_{2-2}\bar{g}\{\tau_0\}/A_{2-1}\bar{g}\{\tau_0/3.35\}$ versus τ_0 . This ratio is equal to the intensity ratio of the C III $2s2p^3P - 2p^2^3P$ 2–2 line over the 1–2 line. Optical depths versus position may be determined by comparison of the observed ratios shown in fig. 2.10a.

Photo-absorption is most likely to occur when the lower level populations are large and long lived – i.e. metastable. Such populations, however, are collisionally controlled and so the relative populations of two metastable levels of an ion are insensitive to opacity and may be determined in an optically thin model, i.e.

$$\tau_{0,l_1 \rightarrow u} = \text{const} \times \tau_{0,l_2 \rightarrow u} \quad (2.24)$$

$$\Rightarrow \tau_{0,l_2 \rightarrow u} = \tau_{0,l_1 \rightarrow u} / \text{const} \quad (2.25)$$

$$\Rightarrow \tau_{0,l_1 \rightarrow u} = R^{-1} \left(\frac{\bar{g}\{\tau_{0,l_1 \rightarrow u}\}}{\bar{g}\{\tau_{0,l_1 \rightarrow u} / \text{const}\}} \right) \quad (2.26)$$

where

$$R(\tau_0) = \bar{g}\{\tau_{0,l_1 \rightarrow u}\} / \bar{g}\{\tau_{0,l_1 \rightarrow u} / \text{const}\} \quad (2.27)$$

Thus optical depth may be deduced directly from observations of spectral line intensities. For example, fig. 2.3 shows $A_{2-2}\bar{g}\{\tau_0\}/A_{2-1}\bar{g}\{\tau_0/3.35\}$ versus τ_0 . Comparison

between this curve and observed values of the I(2-2)/I(1-2) ratio of the C III $2s2p^3P - 2p^2^3P$ multiplet (1175 Å) yields values for $\tau_{0,2-2}$. This is demonstrated in sec. 2.3.

2.2 The effect of opacity on the population structure

It is demonstrated above that in the ratio of lines arising from a common upper level, the term that accounts for the effect of scattering into the line-of-sight disappears. Equivalently, it can be said that this ratio does not depend on the population structure. However, there is an effect on the population structure due to opacity. McWhirter (1965) introduced an escape factor type approach to this problem as follows. The intensity term, \bar{I}_ν in eq. 2.6 for some point in a layer is

$$\bar{I}_\nu = \frac{1}{4\pi} \int_0^{4\pi} I_\nu(\theta, \phi) d\Omega \quad (2.28)$$

where $I_\nu(\theta, \phi)$ is the intensity along a path in the direction (θ, ϕ) and $d\Omega$ is an element of solid angle. $I_\nu(\theta, \phi)$ may be obtained for the constant density case via the solution of the radiative transfer equation, i.e.

$$\begin{aligned} \frac{dI_\nu}{dx} + \kappa_\nu I_\nu &= j_\nu \\ \Rightarrow \frac{d}{dx}(e^{\kappa_\nu x} I_\nu) &= e^{\kappa_\nu x} j_\nu \\ \Rightarrow I_\nu(x) &= \frac{\kappa_\nu}{j_\nu} [e^{\kappa_\nu(L-x)} - e^{-\kappa_\nu x}] \\ \Rightarrow I_\nu = I_\nu(L) &= \frac{\kappa_\nu}{j_\nu} [1 - e^{-\kappa_\nu L}] = \frac{\kappa_\nu}{j_\nu} [1 - e^{-\tau_\nu(\theta, \phi)}] \end{aligned} \quad (2.29)$$

where L is the path length in direction (θ, ϕ) and $\tau_\nu(\theta, \phi) = \kappa_\nu L$. Thus

$$\begin{aligned} \bar{I}_\nu &= \frac{1}{4\pi} \int_0^{4\pi} \frac{\kappa_\nu}{j_\nu} [1 - e^{-\tau_\nu(\theta, \phi)}] d\omega \\ &= \frac{\kappa_\nu}{j_\nu} \overline{[1 - e^{-\tau_\nu(\theta, \phi)}]} \end{aligned} \quad (2.30)$$

where $\overline{1 - e^{-\tau_\nu(\theta, \phi)}}$ is the average of $1 - e^{-\tau_\nu(\theta, \phi)}$ over direction. \bar{I}_ν may be written as

$$\bar{I}_\nu = \frac{\kappa_\nu}{j_\nu} [1 - e^{-\bar{\tau}_\nu(\theta, \phi)}] \quad (2.31)$$

for $\bar{\tau}_\nu = \kappa_\nu \bar{L}$ where \bar{L} is *some representative length*. If it is further assumed, as it was earlier, that the emission and absorption profiles are identical and are purely Doppler broadened, then

$$\frac{\kappa_\nu}{j_\nu} = \frac{N_l \omega_u}{N_u \omega_l} \frac{2\nu_0^2}{c^2} \quad (2.32)$$

From eq. 2.6

$$\Lambda(\mathbf{r}) = 1 - \frac{N_l(\mathbf{r})\omega_u}{N_u(\mathbf{r})\omega_l} \frac{c^2}{2\nu_0^2} \int \bar{I}_\nu(\mathbf{r})\phi(\nu)d\nu \quad (2.33)$$

and thus it follows that

$$\Lambda(\mathbf{r}) = 1 - \frac{1}{\sqrt{\pi}} \int_{-\infty}^{\infty} [1 - \exp\{-\bar{\tau}_0 e^{-u^2}\}] e^{-u^2} du \equiv g\{\bar{\tau}_0\} \quad (2.34)$$

This is a useful result except for the fact that the precise meaning of $\bar{\tau}_0$ is not clear (this is discussed more in sec. 2.6.)

A less ambiguous result may be obtained as follows: consider a plane parallel, semi-infinite layer of constant density and thickness D , and consider a point, $\mathbf{0}$, at its centre. Now consider the intensity, dI_ν at $\mathbf{0}$ due to a volume element, dV , located at the point \mathbf{r} . This may be written as

$$dI_\nu = \frac{j_\nu e^{-\kappa_\nu r}}{r^2} dV \quad (2.35)$$

The intensity, \bar{I}_ν , is then

$$\begin{aligned} I_\nu &= \frac{1}{4\pi} \int \int \int_V \frac{j_\nu e^{-\kappa_\nu r}}{r^2} dV \\ &= \frac{2}{4\pi} \int_0^\pi 2 \int_0^{D/2} \int_x^\infty \frac{j_\nu e^{-\kappa_\nu r}}{r^2} r dr dx d\theta \end{aligned} \quad (2.36)$$

Changing the order of integration yields

$$\begin{aligned} I_\nu &= \int_0^{D/2} \int_0^r \frac{j_\nu e^{-\kappa_\nu r}}{r} dx dr + \int_{D/2}^\infty \int_0^{D/2} \frac{j_\nu e^{-\kappa_\nu r}}{r} dx dr \\ &= \int_0^{D/2} j_\nu e^{-\kappa_\nu r} dr + \frac{d}{2} \int_{D/2}^\infty \frac{j_\nu e^{-\kappa_\nu r}}{r} \\ &= \frac{j_\nu}{\kappa_\nu} \left[1 - e^{-\kappa_\nu D/2} + \frac{\kappa_\nu D}{2} E_1 \left(\frac{\kappa_\nu D}{2} \right) \right] \end{aligned} \quad (2.37)$$

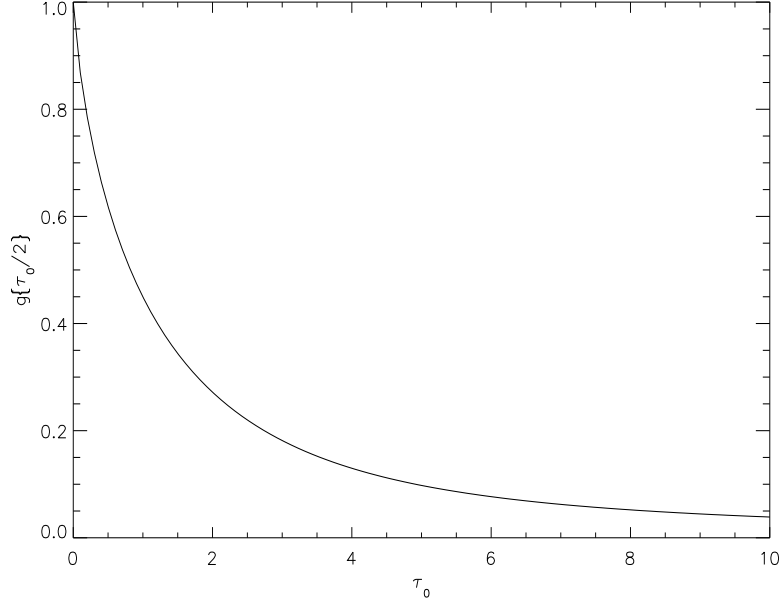


Figure 2.4: Plot of $\bar{g}\{\tau_0/2\}$ versus τ_0 .

where E_1 is the first exponential integral. It follows that

$$\begin{aligned}
 \Lambda(\mathbf{r}) &= 1 - \frac{1}{\sqrt{\pi}} \int_{-\infty}^{\infty} e^{-u^2} \left[1 - e^{-\kappa_\nu D/2} + \frac{\kappa_\nu D}{2} E_1 \left(\frac{\kappa_\nu D}{2} \right) \right] du \\
 &= \frac{1}{\sqrt{\pi}} \int_{-\infty}^{\infty} e^{-u^2} \left[\exp \left\{ \frac{-\kappa_0 e^{-u^2} D}{2} \right\} - \left\{ \frac{\kappa_0 e^{-u^2} D}{2} \right\} E_1 \left\{ \frac{\kappa_0 e^{-u^2} D}{2} \right\} \right] du
 \end{aligned} \tag{2.38}$$

i.e.

$$\Lambda(\mathbf{r}) = \frac{1}{\sqrt{\pi}} \int_{-\infty}^{\infty} e^{-u^2} \left[\exp \left\{ \frac{-\tau_0 e^{-u^2}}{2} \right\} - \left\{ \frac{\tau_0 e^{-u^2}}{2} \right\} E_1 \left\{ \frac{\tau_0 e^{-u^2}}{2} \right\} \right] du \tag{2.39}$$

Thus the absorption factor for a plane parallel slab of constant density may be written purely as a function of the *perpendicular* optical depth and so it is called here $\bar{g}\{\tau_0/2\}$ (Brooks et al., 2000). This expression is the same as that denoted by Bhatia & Kastner (1997) as $SEFD(C, T)$ (which stands for *slab escape factor, Doppler* which

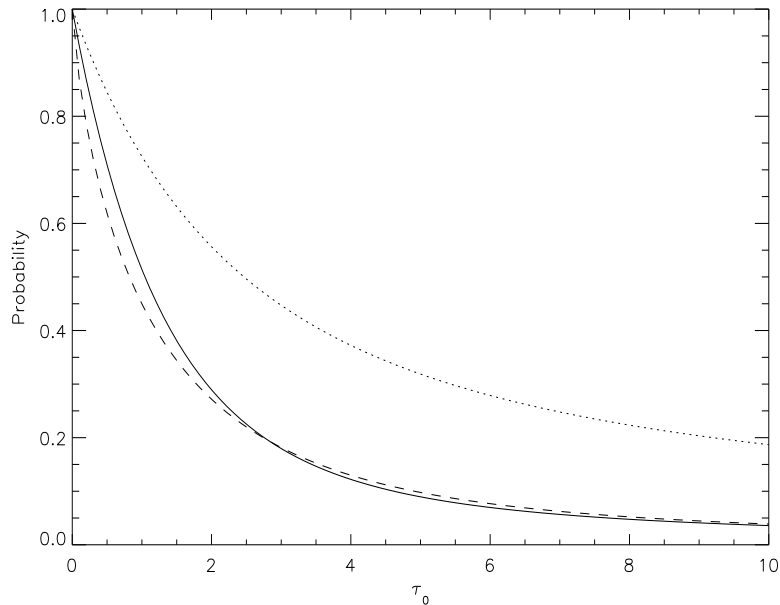


Figure 2.5: Solid line – $g\{\tau_0\}$; dotted line – $\bar{g}\{\tau_0\}$; dashed line – $\bar{g}\{\tau_0/2\}$ versus τ_0 .

is a function of position, C , in the layer and optical depth, T – Bhatia & Kastner’s notation). $\bar{g}\{\tau_0/2\}$ is plotted versus optical depth in fig. 2.4. In fig. 2.5 it is shown in comparison with $g\{\tau_0\}$ and $\bar{g}\{\tau_0\}$ where it can be seen that it is close to $g\{\tau_0\}$. Figs 2.6 and 2.7 show the C III $2p^{23}P_2/2p^{23}P_1$ and $2p^{23}P_2/2s2p^3P_2$ population density ratios respectively, versus optical depth. Both are calculated by including appropriate $\bar{g}\{\tau_0/2\}$ values in the statistical balance equations. The former ratio varies markedly for small values of optical depth but levels off with large values. This is due to the sensitivity of the corresponding $\bar{g}\{\tau_0/2\}$ ratio which is high for small optical depth values and low for large values. Fig. 2.7 illustrates the dependence of the source function of the C III $2s2p^3P_2 - 2p^{23}P_2$ line on optical depth based again on $\bar{g}\{\tau_0/2\}$.

2.2.1 Extrapolation to all transitions of an ion

Since optical depth may be extracted from observation as described above, if this is done for a spectral line at disk centre then the absorption factor is also known for

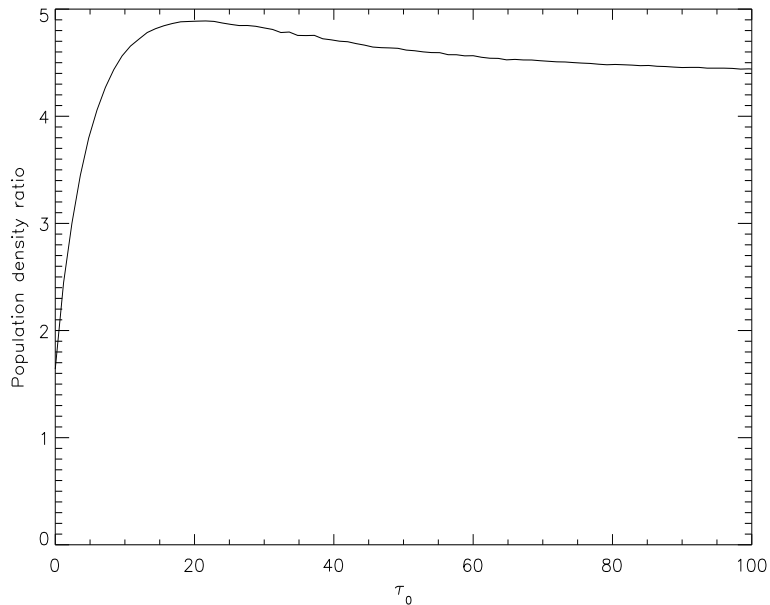


Figure 2.6: Plot of C III $2p^2^3P_2/2p^2^3P_1$ population density ratio versus τ_0 based on $\bar{g}\{\tau_0/2\}$.

that line. As stated earlier in sec. 2.1.1, the spectral lines that are most significantly modified by opacity are those whose lower levels are metastable. These levels are not significantly altered due to their large population densities and are collisionally controlled. Thus the relative population of metastable components is negligibly affected by opacity and may be calculated by solving eq. 2.6 in the optically thin approximation. It follows that optical depths for all lines of an ion whose lower levels are metastable may be deduced via eq. 2.24 from a single optical depth value. If it is assumed that all other optical depths are negligible then all are known for the ion.

2.3 Opacity deduction at the limb of the sun

In September 1996 an observing sequence was run using the SUMER spectrometer on board the SOHO spacecraft. SUMER is a normal incidence extreme ultraviolet (EUV) spectrometer (Wilhelm et al., 1995) with a spatial resolution of ~ 1 arc sec

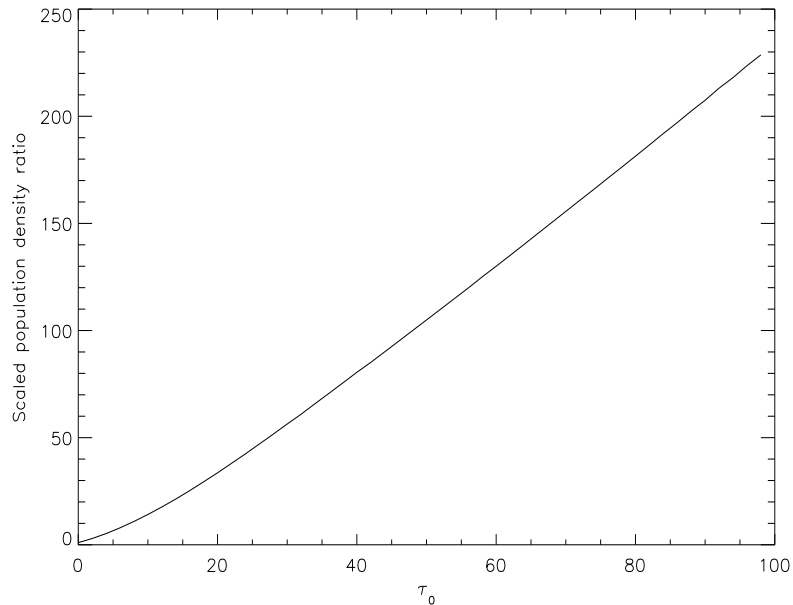


Figure 2.7: Plot of $C \text{ III } 2p^2\ ^3P_2/2s2p^3\ ^3P_2$ population density ratio versus τ_0 based on $\bar{g}\{\tau_0/2\}$. This ratio is scaled so that it is unity for an optical depth of 0. This ratio illustrates the dependence of the source function of the $C \text{ III } 2s2p^3\ ^3P_2 - 2p^2\ ^3P_2$ line on optical depth.

which corresponds to a distance a little less than 1000 km on the sun. The sequence comprised of east-west scans in 18 spatial steps over the west (receding) limb of the sun. Surface plots of the cross-limb data are shown for the $C \text{ II } 904 \text{ \AA}$ and $C \text{ III } 1175 \text{ \AA}$ multiples in fig. 2.8. The limb region was chosen for its great variation in optical depth. It can be seen from eq. 2.16 that the optical depth of a spectral line is proportional to both the lower level population density and the thickness along the line-of-sight of the emitting layer. Thus, thinking of the layer as a spherical shell above the sun's surface, on approaching the limb from the disk the optical depth increases as the line-of-sight thickness increases. On crossing the limb the optical thickness doubles as the portion of the emitting layer on the far side of the sun can be viewed, reaching a maximum when the edge of the emitting layer is reached. After this point, in a stratified atmosphere picture the optical depth decreases rapidly due to the fall off of density with height above the surface.

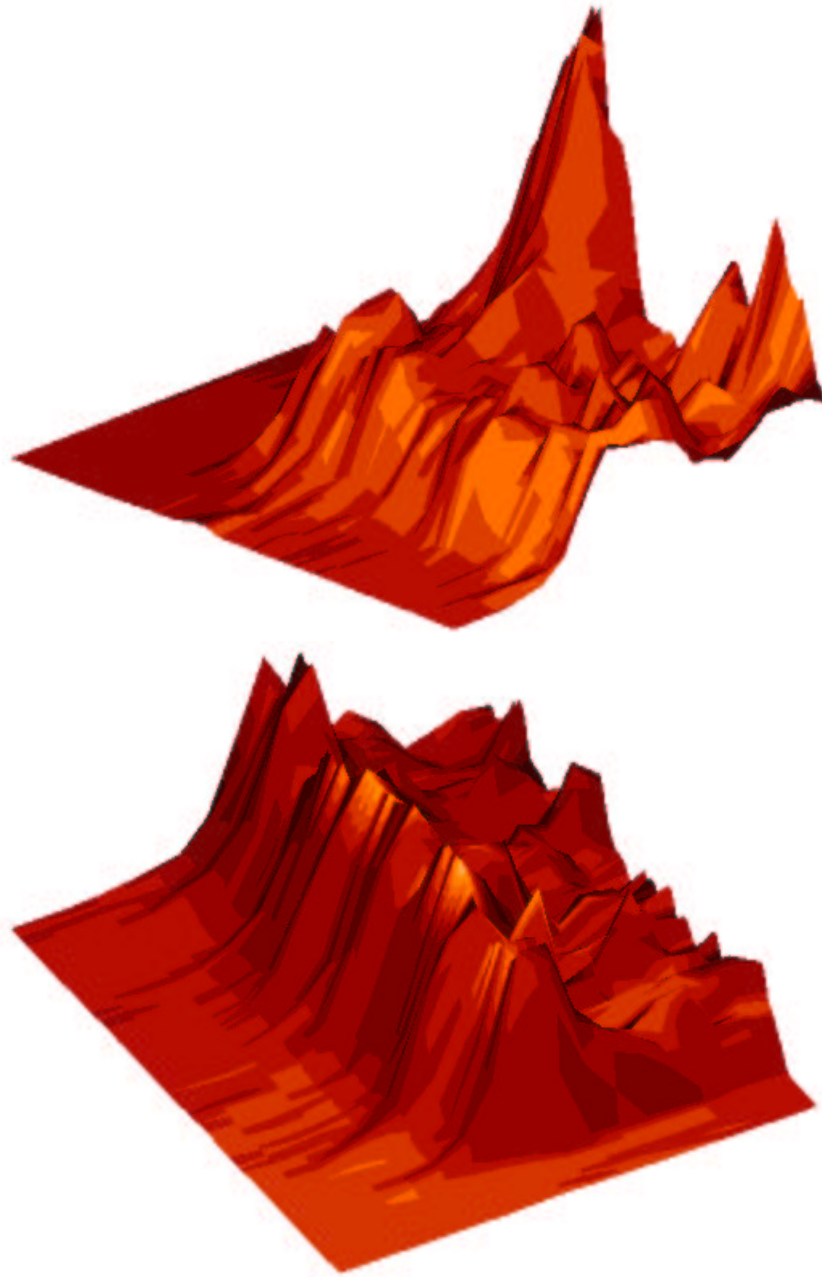


Figure 2.8: Surface plots of total flux in the slit/raster plane for the C II 904 Å (top) and C III 1175 Å (bottom) multiplets. Note that the slit dimension is up and to the left and the raster dimension is down and to the left. The low counts to the extreme left correspond to the off-limb data. The low counts at the top left in the C II case and the bottom right in the C III case are due to un-exposed regions of the detector.

The observed SUMER spectral line fluxes (proportional to intensity) were analysed in the escape probability model described to obtain optical depths for all the spectral lines of C II and C III. The results of this analysis are shown in tables 2.1 → 2.5.

Table 2.1: Summary of data for the C III $2s2p^3P_2 - 2p^2^3P_2$ transition for each raster scan position. $\tau_{0,2-2}/\tau_{0,1-2} = 3.204$

Pos.(")	$\tau_{0,2-2}$	$\bar{g}\{\tau_{0,2-2}\}$	$\bar{\tau}_{0,2-2}$	$g\{\tau_{0,2-2}\}$
943.06	0.74	0.78	0.35	0.79
944.94	0.94	0.74	0.43	0.75
946.81	1.09	0.71	0.49	0.72
948.69	1.27	0.67	0.56	0.67
950.56	1.05	0.71	0.47	0.73
952.44	1.18	0.69	0.53	0.70
954.31	1.86	0.58	0.78	0.60
956.19	3.42	0.41	1.23	0.45
958.06	-	-	3.12	0.17
959.94	-	-	4.24	0.11
961.88	8.64	0.21	2.00	0.29
963.75	1.68	0.60	0.71	0.62
965.63	1.27	0.67	0.56	0.69
967.50	1.42	0.64	0.62	0.66
969.38	1.81	0.58	0.76	0.60
971.25	1.67	0.60	0.71	0.62
973.13	2.24	0.53	0.90	0.55
975.00	2.13	0.54	0.87	0.56

2.4 Atmosphere Modelling

Spectral intervals spanning the C II $2s^2p^2P - 2s2p^2^2S$ multiplet at $\sim 1036 \text{ \AA}$ and the C III $2s2p^3P - 2p^2^3P$ multiplet at $\sim 1175 \text{ \AA}$ are shown in figs 2.9a and 2.10a respectively. The multiplet components are labelled according to their J quantum numbers. Observed flux ratios for the C II $I(3/2-1/2)/I(1/2-1/2)$ ratio and the C III $I(2-2)/I(1-2)$ ratio are shown in figs 2.9b and 2.10b. As stated earlier, in both cases the lines

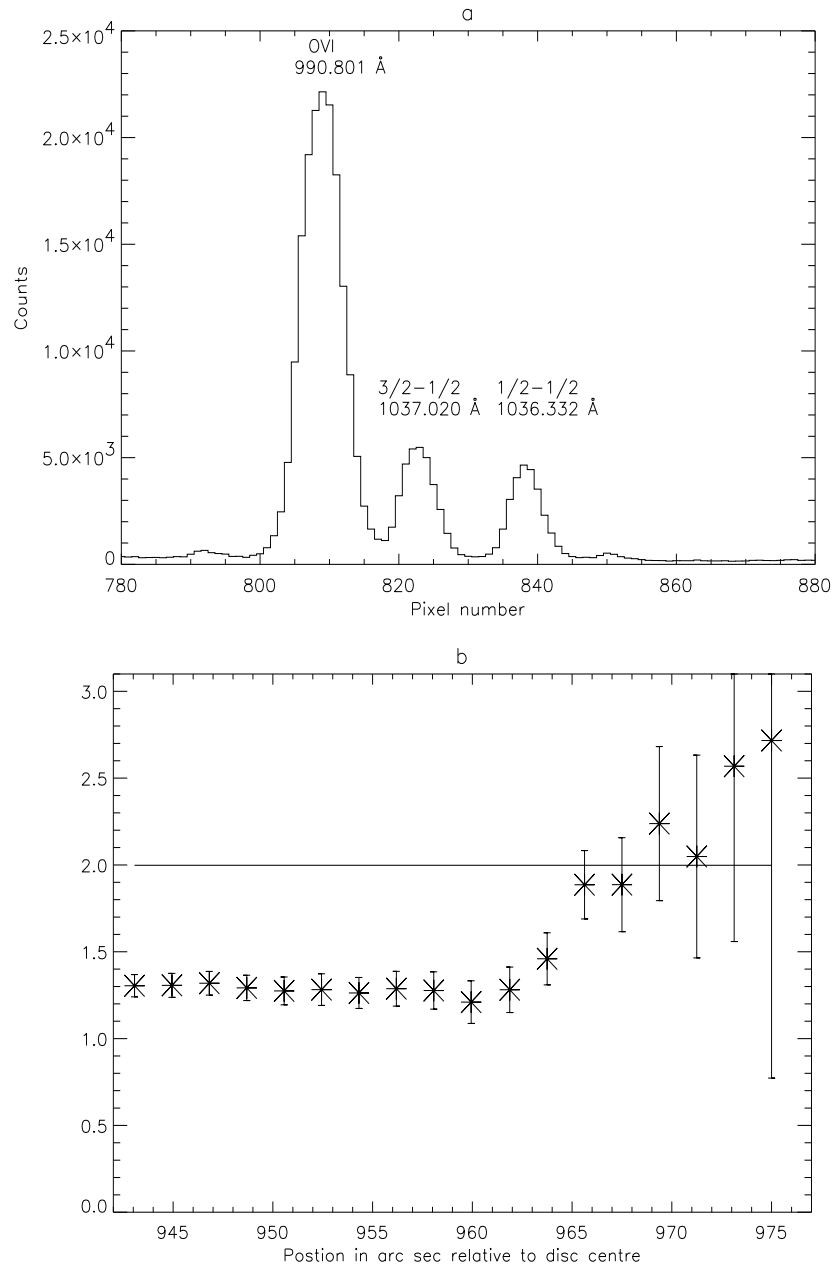


Figure 2.9: (a) Spectral interval spanning the C II $2s^2p^2P - 2s2p^2S$ (1036 Å) multiplet with component identification. The ordinate scale records the number of counts integrated along the line-of-sight and for each pixel along the wavelength scale measured in the 100 sec. of exposure time. (b) Branching line intensity ratios versus raster position in arc sec relative to the disk centre. The set of values correspond to the $I(3/2-1/2)/I(1/2-1/2)$ ratio. The solid line shows the corresponding A-value ratio.

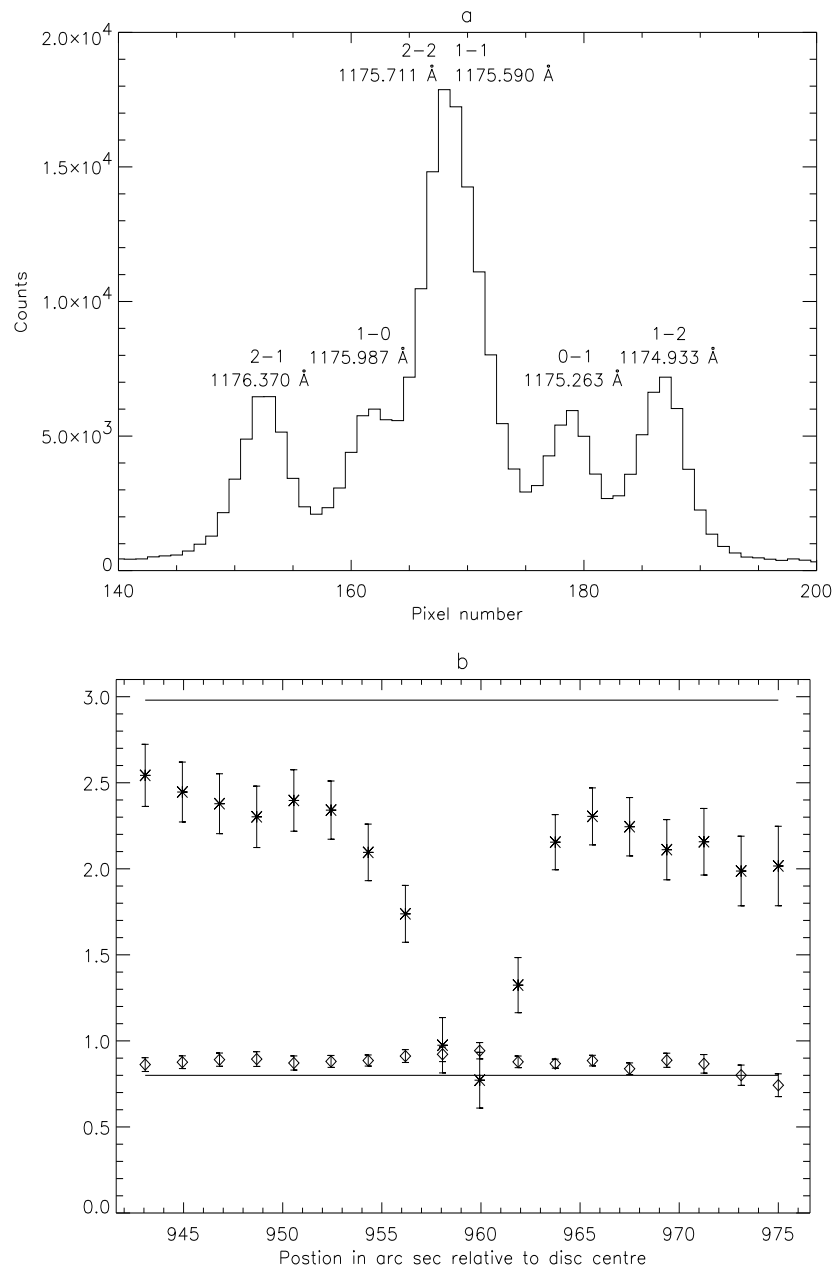


Figure 2.10: a) Spectral interval spanning the C III $2s2p^3P - 2p^2^3P$ (1175 Å) multiplet with component identification. Ordinate scale as in fig. 2.9a. (b) Branching line intensity ratios versus raster position in arc sec relative to the disc centre. The upper set of values (*) correspond to the $I(2-2)/I(1-2)$ ratio and the lower set (◇'s) correspond to the $I(0-1)/I(2-1)$. The solid lines show the corresponding A-value ratios.

Table 2.2: Summary of data for the C III $2s2p\ ^3P_0 - 2p^2\ ^3P_1$ transition for each raster scan position. $\tau_{0,0-1}/\tau_{0,2-1} = 0.779$. Since the optical depth ratio is fairly close to unity, the absolute optical depths inferred here are expected to have large associated errors and would be more reliably obtained from the 2-2 values shown in table 2.1.

Pos.(")	$\tau_{0,0-1}$	$\bar{g}\{\tau_{0,0-1}\}$	$\bar{\tau}_{0,0-1}$	$g\{\tau_{0,0-1}\}$
943.06	0.91	0.77	0.39	0.77
944.94	1.16	0.71	0.48	0.72
946.81	1.47	0.65	0.58	0.68
948.69	1.55	0.64	0.60	0.67
950.56	1.07	0.73	0.45	0.74
952.44	1.25	0.69	0.51	0.71
954.31	1.36	0.67	0.55	0.69
956.19	2.02	0.57	0.72	0.62
958.06	2.34	0.52	0.79	0.59
959.94	3.26	0.44	0.94	0.54
961.88	1.20	0.70	0.50	0.72
963.75	1.00	0.75	0.43	0.75
965.63	1.35	0.66	0.54	0.70
967.50	0.51	0.87	0.24	0.85
969.38	1.39	0.67	0.56	0.69
971.25	0.98	0.75	0.42	0.75
973.13	0.01	1.00	0.00	1.00
975.00	0.00	1.00	0.00	1.00

involved arise from common upper levels and so the ratios do not depend upon the population structure. Thus the ratios are only modified from their optically thin values (shown in each case by a solid horizontal line) due to the scattering of photons out of the line-of-sight. Variations in the ratios therefore reflect variations in optical depth which is, simplistically speaking, linearly dependent on the length of the line-of-sight and on the lower level population density (see eq. 2.16).

Consider first the C III ratio plot (fig. 2.10b). The optical depth ratio of the 0-1 component to the 2-1 component ($\tau_{0,0-1}/\tau_{0,2-1}$) is close to unity. Consequently the escape probability ratio of these two lines is also close to unity for all optical depths. It follows that the corresponding intensity ratio does not deviate significantly from

Table 2.3: Summary of data for the C II $2s^22p\ ^2P_{3/2} - 2s2p^2\ ^2S_{1/2}$ transition for each raster scan position. $\tau_{0,3/2-1/2}/\tau_{0,1/2-1/2} = 1.97$.

Pos.(")	$\tau_{0,3/2-1/2}$	$\bar{g}\{\tau_{0,3/2-1/2}\}$	$\bar{\tau}_{0,3/2-1/2}$	$g\{\tau_{0,3/2-1/2}\}$
943.06	5.30	0.31	1.47	0.39
944.94	5.25	0.31	1.46	0.39
946.81	4.95	0.32	1.42	0.40
948.69	5.70	0.29	1.51	0.38
950.56	6.23	0.27	1.56	0.37
952.44	6.00	0.28	1.54	0.37
954.31	6.70	0.26	1.60	0.36
956.19	5.80	0.29	1.52	0.38
958.06	6.20	0.27	1.56	0.37
959.94	10.2	0.18	1.80	0.32
961.88	6.00	0.28	1.54	0.37
963.75	2.82	0.46	1.03	0.50
965.63	0.36	0.88	0.17	0.89
967.50	0.36	0.88	0.17	0.89
969.38	-	-	-	-
971.25	-	-	-	-
973.13	-	-	-	-
975.00	-	-	-	-

the optically thin value on crossing the limb. However, the $\tau_{0,2-2}/\tau_{0,1-2}$ ratio is ~ 3 and so the intensity ratio $I(2-2)/I(1-2)$ is opacity sensitive. On disk the emitting layer is only moderately thick and so the observed flux ratios are close to their optically thin value. As the limb is approached the ratios deviate markedly from their thin value due to the variation of optical depth with line-of-sight thickness, as discussed in sec. 2.3. This deviation is most pronounced at the position of the visible limb (~ 959.6 arc sec) where the line-of-sight doubles in length. The ratio continues to drop until the inner edge of the emitting layer is reached (~ 964 arc sec) whereafter it rises again toward the thin value. In a stratified atmosphere picture, this rise is due to the fall off of density with height above the solar surface. The ratios do not return to their optically thin value as might be expected but rather level off at a value similar to

Table 2.4: Summary of data for the C II $2s^22p\ ^2P_{3/2} - 2s2p^2\ ^2P_{1/2}$ transition for each raster scan position. $\tau_{0,3/2-1/2}/\tau_{0,1/2-1/2} = 0.507$. The opacity ratio is again fairly close to unity and the comments on table 2.2 apply.

Pos.(")	$\tau_{0,3/2-1/2}$	$\bar{g}\{\tau_{0,3/2-1/2}\}$	$\bar{\tau}_{0,3/2-1/2}$	$g\{\tau_{0,3/2-1/2}\}$
943.06	0.66	0.80	0.29	0.83
944.94	0.47	0.85	0.21	0.87
946.81	0.31	0.90	0.14	0.91
948.69	0.12	0.96	0.06	0.97
950.56	0.33	0.89	0.15	0.91
952.44	0.49	0.85	0.22	0.87
954.31	0.47	0.85	0.21	0.87
956.19	0.19	0.94	0.09	0.95
958.06	0.43	0.86	0.20	0.88
959.94	0.33	0.89	0.15	0.91
961.88	0.39	0.87	0.18	0.89
963.75	0.12	0.96	0.06	0.97
965.63	0.14	0.95	0.07	0.97
967.50	0.10	0.97	0.05	0.98
969.38	1.50	0.63	0.54	0.70
971.25	1.47	0.64	0.53	0.70
973.13	8.46	0.21	0.99	0.52
975.00	-	-	1.41	0.40

that on disk. A plot of observed flux of the C III $2s2p^3P_2 - 2p^2^3P_2$ line at 1175.711 Å versus position is shown in fig. 2.11. It is clear that at the heights above 967 arc sec where the ratios indicate that the lines are thick, the fluxes are very small and so it is possible that the observed signal is dominated by instrumentally scattered light – light that reflects off the interior of the telescope prior to passing through the entrance slit. Instrumentally scattered light originates from points on the solar disk and thus it would be reasonable to expect such light to imply opacities associated with the disk. This idea is supported by the fitted centroid positions of the C III 1175 Å multiplet components which are shown in fig. 2.12. The overlapped 2–2 and 1–1 components are awkward to fit, especially at the limb where the optical depths are greatest and thus the deviation due to opacity of line-shapes from Gaussian is most significant.

Table 2.5: Summary of data for the C II $2s^22p^2P_{3/2} - 2s2p^2^2P_{3/2}$ transition for each raster scan position. $\tau_{0,3/2-3/2}/\tau_{0,the1/2-3/2} = 5.05$.

Pos.(")	$\tau_{0,3/2-3/2}$	$\bar{g}\{\tau_{0,3/2-3/2}\}$	$\bar{\tau}_{0,3/2-3/2}$	$g\{\tau_{0,3/2-3/2}\}$
943.06	4.95	0.32	1.64	0.36
944.94	5.01	0.32	1.65	0.35
946.81	4.13	0.36	1.46	0.39
948.69	4.37	0.35	1.51	0.38
950.56	5.15	0.31	1.68	0.35
952.44	4.81	0.33	1.61	0.36
954.31	4.56	0.34	1.55	0.37
956.19	5.23	0.31	1.69	0.34
958.06	5.10	0.31	1.67	0.35
959.94	4.69	0.33	1.58	0.37
961.88	4.84	0.33	1.61	0.36
963.75	4.40	0.35	1.52	0.38
965.63	2.88	0.46	1.13	0.48
967.50	2.36	0.51	0.96	0.53
969.38	1.07	0.71	0.49	0.72
971.25	1.40	0.65	0.62	0.66
973.13	1.63	0.61	0.71	0.62
975.00	1.29	0.67	0.58	0.68

As such, a wavelength direction pixel shift vector was imposed, determined from the centroid positions of the well separated 2–1 and 1–2 multiplet components. It can be seen from fig. 2.12 that beyond the limb, at a height of around 967.50 arc sec, the centroids are shifted to the blue indicative of upflows along the line-of-sight of ~ 20 km/s. The onset of this shift is beyond the visible limb (959.6 arc sec) and the inner edge of the C III emitting layer (~ 962 arc sec) and coincides with the point at which the model ratios (fig. 2.16b – see sec. 2.4.1) begin to deviate from the observed ones. If this is the case then the scattered light – which is a whole disk integrated effect – has a blue shift relative to the limb observations of ~ 20 km/s. This is in contrast to observations of emission at TR temperatures which show that downflows with similar speeds are dominant on the disk (Athay and Holzer, 1982; Brekke et al.,

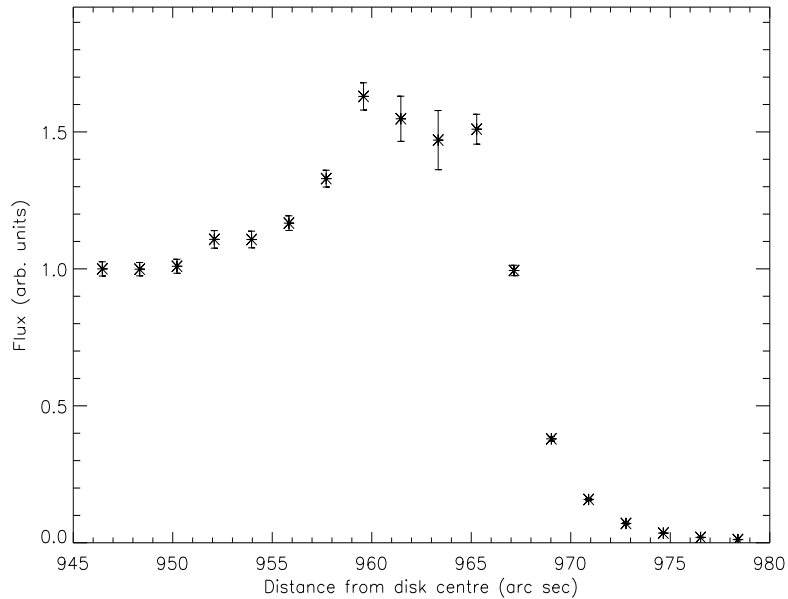


Figure 2.11: Integrated line fluxes for the C III $2s2p^3P_2 - 2p^2^3P_2$ line at 1175.711 Å. Ordinate scale as in fig. 2.9a.

1997; Chae et al., 1998).

An alternative explanation follows if the signals at such heights are in fact true. At heights above 967 arc sec the fluxes imply smaller column densities than those on disk since the intensity is proportional to the upper level column density (see eq. 2.15). However, the ratios suggest that the column densities at such heights are comparable with those on disk, since the ratios follow the optical depth variation which is determined by that of the lower level column density (see eq. 2.16). These seemingly contradictory implications are reconciled if the *filling factor* changes with height. That is, if there are structures above 964 arc sec which are unresolved in observations. In order to settle this issue the expected contribution of scattered light must be carefully considered (see chap 6).

The C II ratios (fig. 2.9b) differ from those of C III. On disk their value is markedly different to the optically thin value and on approaching and crossing the limb the ratio changes little. The reason for this is that the C II line optical depths are greater than 1

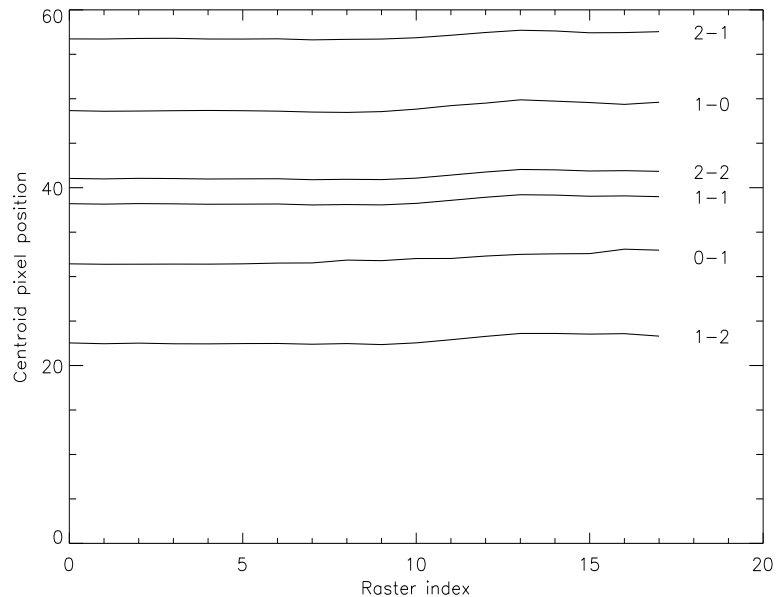


Figure 2.12: Centroid pixel positions for the C III $2s2p^3P - 2p^2^3P$ multiplet components.

prior to the limb and so light emitted at the inner edge of the layer does not have a significant probability of escaping the layer along the line-of-sight. In other words, the layer can only partially be ‘seen’. Thus as the layer thickens with height the visible portion does not change and so the thickening of the line-of-sight makes little difference. Upon crossing the inner edge of the emitting layer (at ~ 961 arc sec), as in the C III case, the ratio rises toward the optically thin value. No comment can be made here on the issue of scattered light due to the large error bars.

2.4.1 Modelling flux ratios on disk

In this chapter stratified atmosphere models are considered. Consequently two distinct regimes exist, one where the opacity variation is principally determined by the geometric extension of the line-of-sight and another where the density fall off with height is determinate. Two models are constructed: the first describes the former

regime and thus deals purely with the observations up to the inner edge of the emitting layer situated a few arc sec above the limb and is termed the *inner* model; the second describes the latter regime and thus regions above the emitting layer edge and is termed the *outer* model.

Following Doyle & McWhirter (1980 – hereafter referred to as DM), the inner model is made up of a spherical shell of constant density. In this picture the optical depth is proportional to $1/\cos\theta$ where θ is 0 at disk centre and $\pi/2$ at the inner edge of the emitting layer. Specifically $\tau_0 = \tau_{0,dc} \times \delta/\cos\theta$ where $\tau_{0,dc}$ is the optical depth at disk centre. $\delta = 1$ before the visible limb and 2 beyond it, and accounts for the doubling in length of the line-of-sight at the limb since the emitting layer on the far side of the sun may be viewed beyond this point.

Using this expression for optical depth, models of the flux ratios for the C II and C III ratios shown in figs 2.9b and 2.10b, were calculated using equation 2.22. The fit to the C III ratios, shown in fig. 2.13(a), reveals a pointing error of ~ 3.4 arc sec. This is consistent with the positional error in SUMER which is ~ 10 arc sec. The fit to the C II fit is shown in fig. 2.14. Also shown are the results obtained using $g\{\tau_0\}$ rather than $\bar{g}\{\tau_0\}$. The former quantity was used by DM and its use is discussed in sec. 2.6.

2.4.2 Modelling flux ratios beyond the limb

It is expected that beyond the limb the opacity variation will be determined by the fall off of density. The model thus far is of a static stratified atmosphere. In such an atmosphere there is both energy and pressure balance and through consideration of these, the temperature and electron density versus height may be determined. Therefore emission following the $G(T_e)$ function¹ with a TR layer as described above is considered. T_e and N_e follow the VAL quiet sun atmosphere model. The optical depth for a given height, h , above the surface, is then

¹The $G(T_e)$ function describes the emission from a particular transition as a function of electron temperature.

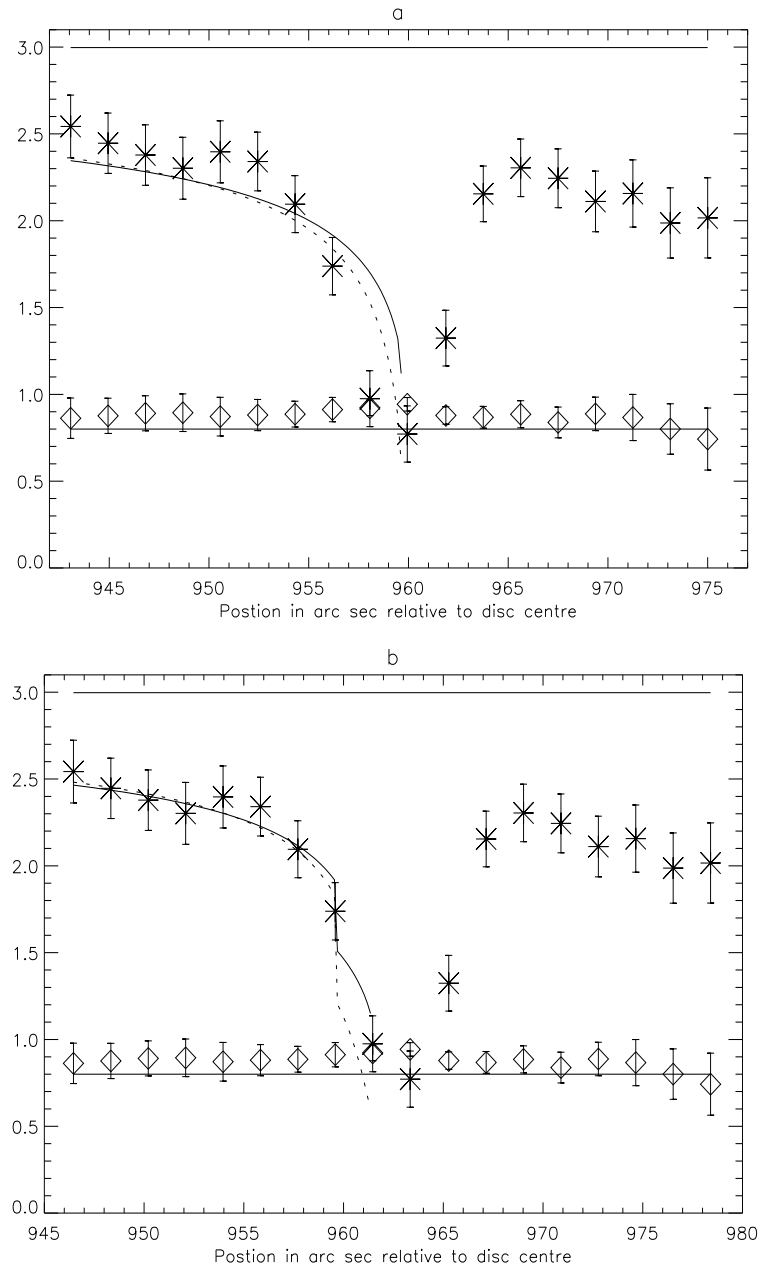


Figure 2.13: Observed branching line intensity ratios versus raster position in arc sec relative to the disk centre for the $C\text{ III } 2s2p^3P - 2p^2\ ^3P$ ($1175\ \text{\AA}$) multiplet component ratios $I(2-2)/I(1-2)$ and $I(0-1)/I(2-1)$ as in fig. 2.10b. Inner model values using $\bar{g}\{\tau_0\}$ (solid line) and $g\{\tau_0\}$ (dashed line) are overlaid. The x-axis uses the position for the visible limb (a) from the telemetry and (b) from an optimised fit of the model to the observed $I(2-2)/I(1-2)$ ratio values.

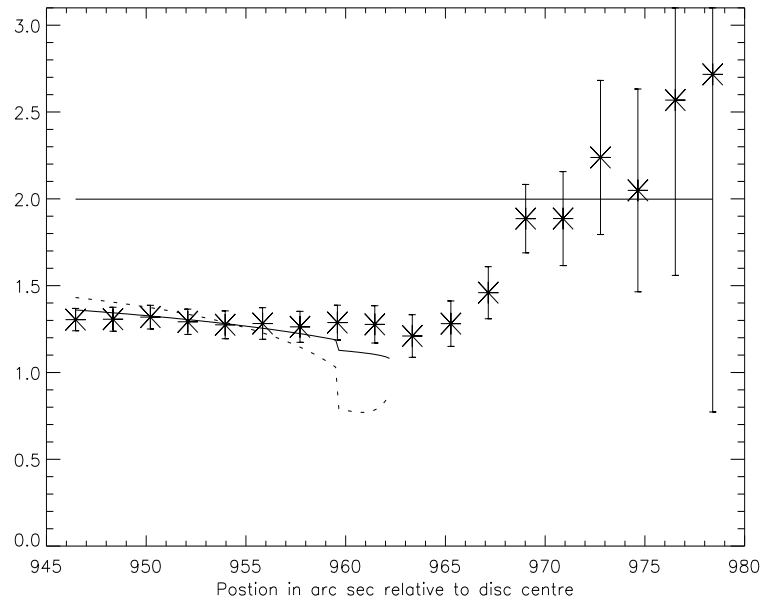


Figure 2.14: (a) Calculated intensity ratios for the C II $2s^2p^2P - 2s2p^2^2S$ (1036 Å) multiplet component ratios $I(3/2-1/2)/I(1/2-1/2)$ versus raster position in arc sec relative to the disc centre compared with the observed ratios. Solid and dashed lines are as in fig. 2.13.

$$\begin{aligned}
 \tau(h) &= a \int_{l.o.s.} N_l(h) ds \\
 &= b \int_{l.o.s.} N_e(h) \bar{G}_{u \rightarrow l}(h) ds
 \end{aligned} \tag{2.40}$$

where $\bar{G}_{u \rightarrow l}(h) \equiv G_{u \rightarrow l}(T_e(h))$, a and b are constants and *l.o.s.* stands for *line-of-sight*. Using this and eq. 2.22, the ratio variations for C II and C III may be modelled. The results of this model can be seen in figs 2.15a and b which clearly demonstrate that the model fails completely. The results of the model follow intuitively from consideration of fig. 1.7 which predicts a very narrow TR of only a few hundred kilometres width. Thus the ratios, in such a picture, move from thick to thin in less than 1 arc sec. This failure of the VAL model is not surprising when one considers images such as figs 2.8a and b which demonstrate that the TR is far from homogeneous.

The failure here does not invalidate the VAL model as such, but, rather, implies

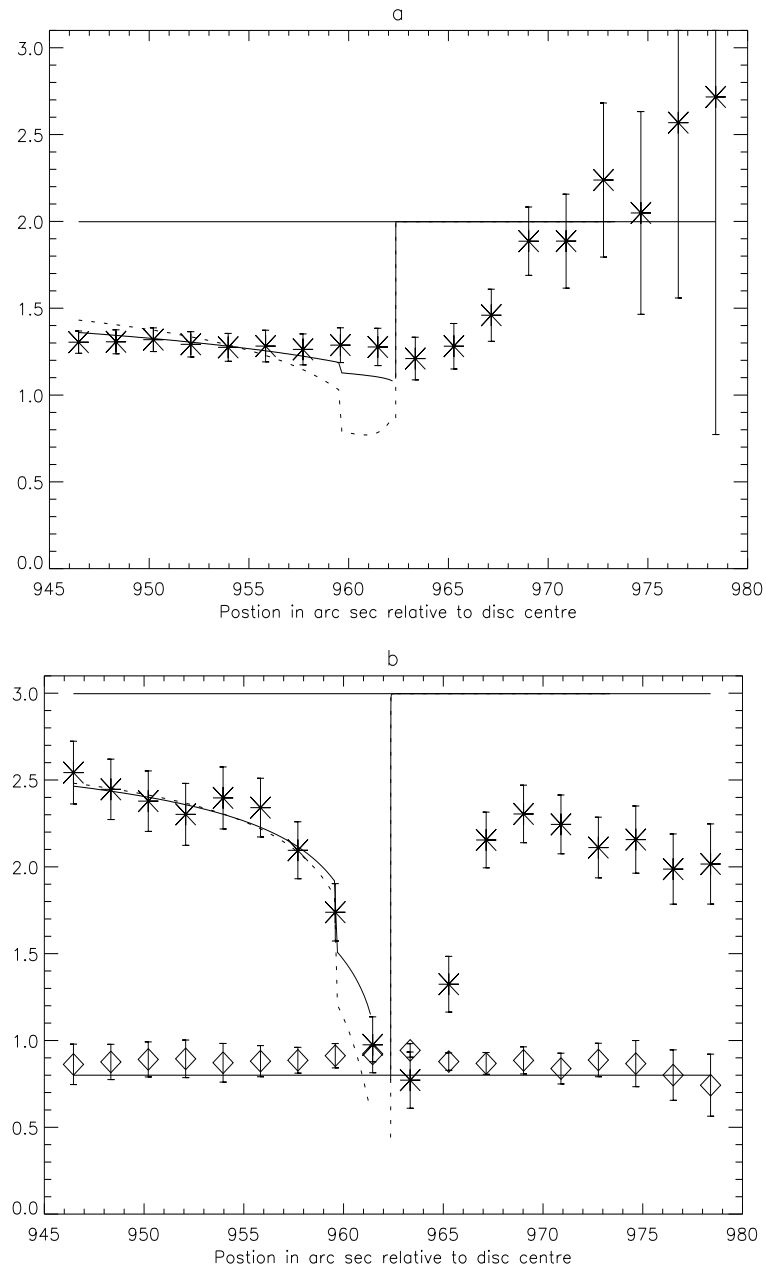


Figure 2.15: Observed branching line intensity ratios versus raster position in arc sec relative to the disk centre for the (a) C II I(3/2-1/2)/I(1/2-1/2) ratio as in fig. 2.9 and (b) C III I(2-2)/I(1-2) ratio as in figs 2.10 and 2.13. The results of the VAL based model are overlaid. The solid line curves show the $\bar{g}\{\tau_0\}$ based results and the dashed line shows the $g\{\tau_0\}$ based results.

that the assumption of stratification is ineffective beyond the limb. It is useful to take account of the extension of the TR into the corona due to structures such as spicules within retaining the stratified atmosphere picture.

Although in a stratified atmosphere the variation of opacity above the limb is not principally determined by the geometric variation in the line-of-sight, its length features significantly in the determination of the optical depth by way of the variation with height of what is called here the *line-of-sight filling factor*. The latter is the number of structures intersected by the line-of-sight. It is possible to handle this within a stratified model via an appropriate choice of density profile. Two further models are therefore considered: firstly, following the approach of Kastner and Bhatia (1992), an emission layer of constant (adjustable) thickness and density is envisaged. This model is a simple parametric adjustment which does not attempt to capture anything of the nature of the spicule structures. Nevertheless, it is useful to consider such a model in order to put the success of any other simple model in context. Secondly, a layer of density which falls off exponentially with adjustable scale height is envisaged. That is, the density falls off as $Be^{-x/H}$ for some constants H and B . This is motivated by the findings of Mariska et al. (1978) who considered models where the dominant contribution to the EUV signal was due to TR sheaths around isolated cylindrical $H\alpha$ spicules. They showed that ‘above the emission peak the amount of emitting material in the line-of-sight for any spectral line must decrease exponentially with height with a scale height that depends on temperature’. This is identical, in essence if not in approach, to the model of Withbroe & Mariska (1976). In summary the models considered are

1. Thin TR based on the VAL atmosphere model
2. Spherical shell of constant density
3. Layer of density that falls off exponentially with height

The results of these models are shown in figs 2.16a and b from which it is clear that both models 2 and 3 are much more effective than the VAL model. Both capture qualitatively the ratio variation as it increases toward the optically thin limit, with

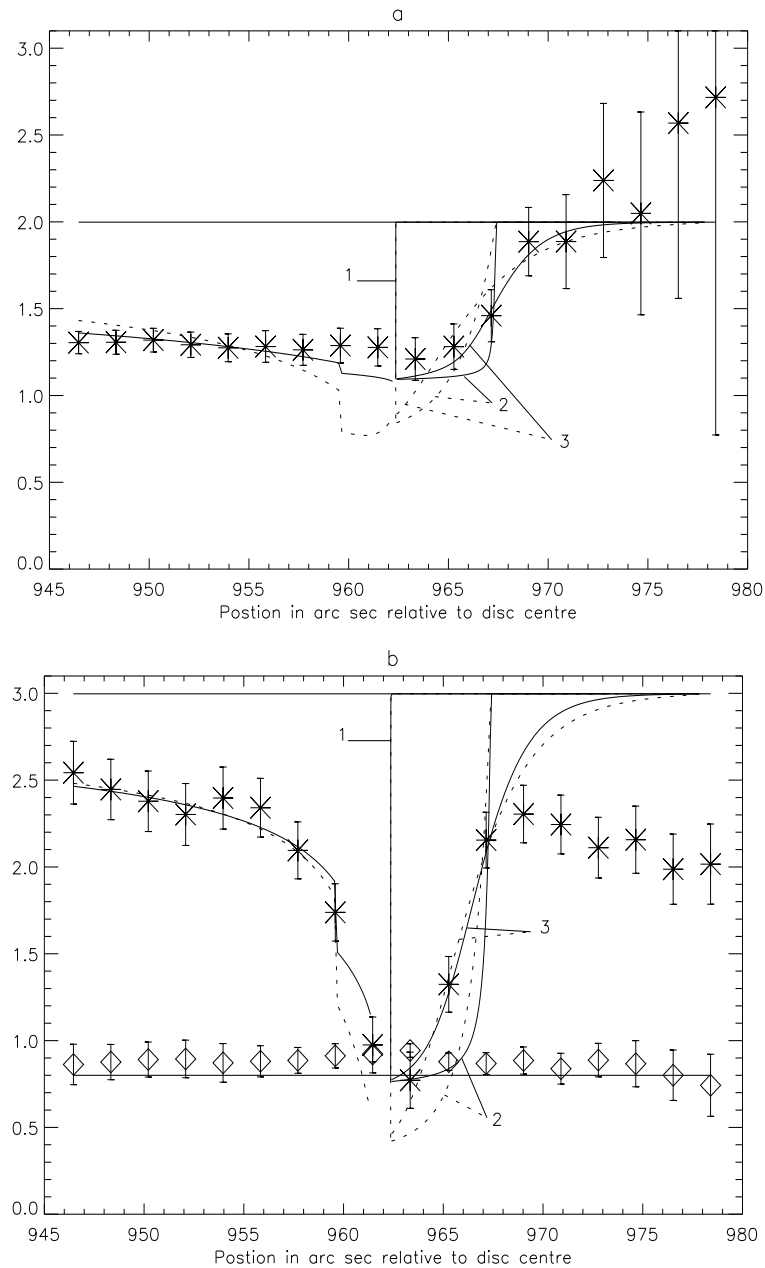


Figure 2.16: Observed branching line intensity ratios versus raster position in arc sec relative to the disk centre for the (a) C II I(3/2-1/2)/I(1/2-1/2) ratio as in fig. 2.15a and (b) C III I(2-2)/I(1-2) ratio as in fig. 2.15b. The results of all three models are overlaid. The solid line curves show the $\bar{g}\{\tau_0\}$ based results and the dashed line shows the $g\{\tau_0\}$ based results. The off-limb models are numbered corresponding to the specification in sec. 2.4.2. The best fit in each case is achieved with the exponential density model and using $\bar{g}\{\tau_0\}$.

the latter model being the most effective in this regard. Both verify the intuitive expectation that the ratio should return to the optically thin value at large heights.

The inner model was optimised for both the optical depth at disk centre and the position of the visible limb. The outer models were optimised for the layer thickness in the constant density case and scale height in the exponential case. The models begin at the inner edge of the emitting layer which is estimated from the height corresponding to the temperature of the peak of the $G(T_e)$ function, obtained from the VAL model. The optical depth at this height is chosen to be consistent with the inner model. The optimised disk centre optical depths were 0.643 for the C II 3/2–1/2 line and 0.156 for the C III 2–2 line respectively. The optimised thickness in model 2 was 5 arc sec for both C II and C III and the scale heights obtained for model 3 were 1.3 arc sec and 1.4 arc sec respectively, equivalent to 942 km and 1015 km. These are smaller than, but comparable to, those suggested by Mariska et al. (1978) (~ 1.5 arc sec) and decrease with decreasing temperature of line formation. These deduced disk centre optical depths allow the spectral lines of C II and C III to be classified according to their optical thickness at disk centre and at the limb. Since it is the disk centre (perpendicular) optical depth that is used within $\bar{g}\{\tau_0/2\}$, this classification includes the effect of opacity upon the population structure.

It is interesting to note that the optimised disk centre optical depth for the C III 2–2 line using $g\{\tau_0\}$ is 0.069 which compares with a value of 0.068 obtained by DM using the same method applied to *Skylab* data.

2.5 Spectral line classification

It is useful to classify spectral lines according to the influence of opacity on both emergent fluxes and on level populations. Such a classification will in general be dependent upon position and time but in the first instance it is useful to consider the quiet sun at disk centre as representative. This classification is pertinent to *differential emission measure* (DEM) studies which allow the *amount of plasma* as a function of electron temperature to be deduced directly from measurements of spectral intensities (Craig & Brown, 1973). Such studies assume optically thin conditions and so using

the escape probability tools described, opacity modified spectral lines may be rejected or intensity adjusted for use in DEM studies.

The modification to emergent fluxes is line-of-sight dependent and so the classification is made according to modifications both at disk centre and at the limb. In contrast, the effects on the population structure are specified by disk centre (perpendicular) optical depths only. The upper level population density of a spectral line may be modified *directly* due to absorption in that same line or *indirectly* due to absorption in another line. As such the spectral lines of an ion may be grouped into the following categories:

1. optically thin (t) – emergent fluxes unmodified on-disk and at the limb; populations unmodified
2. modified thin (mt) – emergent fluxes unmodified on-disk and at the limb; populations indirectly modified
3. weakly thin (wt) – emergent fluxes unmodified on-disk but modified at the limb; populations unmodified
4. modified weakly thin (mwt) – emergent fluxes unmodified on-disk but modified at the limb; populations indirectly modified
5. modified (m) – emergent fluxes modified on-disk and at the limb; populations modified

To do this, for each line two numbers are required: the optical depth at disk centre, $\tau_{0,dc}$, and the optical depth at the limb, $\tau_{0,l}$. These may be deduced for every transition of an ion from just two values, as described in sec. 2.2.1. Consequently only two numbers are required from which a classification may be obtained for every line.

This was done for lines of C II and C III using the optical depths extracted from the OPAC data. A 10% alteration to the Einstein A-coefficient was chosen as the modification criterion. Since $\bar{g}\{\tau_0\} < 0.9$ for $\tau_0 > 0.307$ and $\bar{g}\{\tau_0/2\} < 0.9$ for $\tau_0 > 0.072$ the classification becomes

1. optically thin (t) – $\tau_0 < 0.307$ at the limb, populations unmodified

2. modified thin (mt) – $\tau_0 < 0.307$ at the limb, populations indirectly modified
3. weakly thin (wt) – $\tau_0 < 0.072$ on disk, $\tau_0 > 0.307$ at the limb, populations unmodified
4. modified weakly thin (mwt) – $\tau_0 < 0.072$ on disk, $\tau_0 > 0.307$ at the limb, populations indirectly modified
5. modified (m) – $\tau_0 > 0.072$ on disk

Direct population modification is evident immediately from the optical depth – $\tau_0 > 0.072$ on disk. Indirect population modification, however, is only evident from an optically thick population calculation. In this case a 10% modification in the population was taken as the criterion for modification.

The results for some of the lines of C II and C III are shown in tables 2.6 and 2.7.

2.6 The use of $g\{\tau_0\}$ versus $\bar{g}\{\tau_0\}$

Also featuring in figs 2.16a and b are the results based on $g\{\tau_0\}$ rather than $\bar{g}\{\tau_0\}$. To see how they compare, recall eq. 2.7 and use the intermediate value theorem so that

$$\bar{I} = (1/4\pi)A_{u \rightarrow l}N_u g\{\bar{\tau}_0\}L \quad (2.41)$$

where $\bar{\tau}_0$ is some value of τ_0 such that $0 \leq \bar{\tau}_0 < \tau_0$. This approach mimics that of McWhirter (1965) in the consideration of the absorption factor, described in sec. 2.2. From this it is evident that the DM analysis requires that $\bar{\tau}_0$ replaces τ_0 and $g\{\bar{\tau}_0\}$ replaces $\bar{g}\{\tau_0\}$. However, a question arises as to the definition of $\bar{\tau}_0$. It can be written that $\bar{\tau}_0 = \Delta(\tau_0)\tau_0$. For $\tau_0 < 1$ it can be seen from fig. 2.2 that $\Delta \approx 1/2$ which is to say that the *mean* probability of escape from a layer of optical depth less than unity is equivalent to the probability of escape from the centre of the layer. However, it can also be seen from Fig. 2.2 that for optical depths larger than unity, $\Delta < 1/2$ as

Table 2.6: Characterisation and classification of some spectral lines of C II at disk centre.

Line	$\lambda(\text{\AA})$	f	τ_0	$\bar{g}(\tau_0/2)$	$\bar{g}(\tau_0)$	Class
$2s^2 2p^2 P - 2s 2p^2 D$						
3/2-5/2	1335.709	0.115	0.628	0.638	0.812	m
1/2-3/2	1334.524	0.128	0.353	0.732	0.887	m
3/2-3/2	1335.665	0.027	0.147	0.842	0.950	m
$2s^2 2p^2 P - 2s 2p^2 S$						
3/2-1/2	1037.012	0.129	0.643	0.634	0.808	m
1/2-1/2	1036.332	0.131	0.330	0.742	0.893	m
$2s^2 2p^2 P - 2s 2p^2 P$						
3/2-3/2	904.143	0.405	1.760	0.433	0.590	m
1/2-1/2	903.958	0.331	0.727	0.611	0.787	m
3/2-1/2	904.481	0.0798	0.347	0.734	0.888	m
1/2-3/2	903.620	0.163	0.358	0.730	0.885	m
$2s^2 2p^2 P - 2s^2 3s^2 S$						
3/2-1/2	858.560	0.00615	0.0254	0.956	0.991	mwt
1/2-1/2	858.089	0.00404	0.00843	0.982	0.997	t
$2s^2 2p^2 P - 2s^2 3d^2 D$						
3/2-5/2	687.346	0.282	0.932	0.565	0.740	m
1/2-3/2	687.051	0.270	0.451	0.694	0.859	m
3/2-3/2	687.353	0.025	0.0826	0.893	0.972	m

Table 2.7: Characterisation and classification of some spectral lines of C III at disk centre.

Line	$\lambda(\text{\AA})$	f	τ_0	$\bar{g}\{\tau_0/2\}$	$\bar{g}\{\tau_0\}$	Class
<i>2s2p ³P – 2p² ³P</i>						
2-2	1175.711	0.221	0.156	0.836	0.947	m
1-1	1175.590	0.0713	0.0286	0.9521	0.990	mwt
2-1	1176.370	0.0715	0.0505	0.925	0.983	mwt
1-0	1175.987	0.0913	0.0366	0.942	0.987	wt
1-2	1174.933	0.1176	0.0471	0.929	0.984	mwt
0-1	1175.263	0.2792	0.0393	0.938	0.987	mwt
<i>2s2p ³P – 2s3s ³S</i>						
2-1	538.312	0.031	0.0100	0.979	0.997	wt
1-1	538.149	0.031	0.00569	0.987	0.998	t
0-1	538.075	0.031	0.00200	0.995	1.000	t
<i>2s2p ³P – 2s3d ³D</i>						
2-3	459.627	0.434	0.120	0.862	0.959	m
1-2	459.514	0.394	0.0617	0.914	0.979	wt
0-1	459.466	0.525	0.0289	0.951	0.990	wt
2-2	459.633	0.063	0.0174	0.968	0.994	wt
1-1	459.516	0.100	0.0157	0.970	0.995	wt
2-1	459.635	0.0042	0.00116	0.997	1.000	wt
<i>2s² ¹S – 2s2p ¹P</i>						
0-1	977.020	0.746	0.665	0.628	0.802	m
<i>2s² ¹S – 2s3p ¹P</i>						
0-1	386.203	0.220	0.0775	0.898	0.973	m
<i>2s² ¹S – 2s4p ¹P</i>						
0-1	310.170	0.016	0.00453	0.989	0.999	t

expected since for layers of optical depth greater than 1 not all of the layer is ‘seen’. The implication for the optical depth deduction from this is that

$$\frac{\bar{\tau}_{0,l_1-u}}{\bar{\tau}_{0,l_2-u}} = \frac{\tau_{0,l_1-u}}{\tau_{0,l_2-u}} \frac{\Delta(\tau_{0,l_1-u})}{\Delta(\tau_{0,l_2-u})} \neq \text{constant} \quad (2.42)$$

and the use of $g\{\tau_0\}$ instead of $\bar{g}\{\tau_0\}$ is inappropriate for optical depths greater than 1.

2.7 Concluding remarks

Opacity presents a sizeable problem in modelling and understanding spectral emission from optically thick plasmas. In principle the problem demands the full solution of the coupled non-linear sets of equations of radiative transfer and statistical balance (eqs 2.1 and 2.2). The escape probability quantities, $\bar{g}\{\tau_0\}$ (eq. 2.17) and $\bar{g}\{\tau_0/2\}$ (eq. 2.39) – both purely functions of single optical depths – provide a simple route to linearising and decoupling the equations based on a number of assumptions. These assumptions are that the density is constant in space and that the source function (j_ν/κ_ν) is constant with respect to both space and frequency. Implicit within the latter assumption is that spectral line profiles are Gaussian, that frequency redistribution is complete and there is no line blending. The validity of $\bar{g}\{\tau_0/2\}$ also requires the plasma geometry to be that of a semi-infinite plane parallel slab. The simplicity of this approach allows for the deduction of spectral line optical depths directly from observations of branching line ratios and the extrapolation to all other lines of the ion in question. In addition, when coupled with simple atmosphere models it is possible to extract plasma parameters such as density scale heights and disk centre optical depths. The latter are required to assess the influence of opacity upon the population structure and thus lines have been classified according to line-of-sight attenuation and the modification to the population densities of the levels from which they stem.

It is clear that the escape probability techniques, coupled with the exponential density model, are effective in modelling the observed branching ratio variations in the lines of both C II and C III. However, consideration of the observed fluxes of the C III $2s2p^3P_2 - 2p^2^3P_2$ line at 1175.711 Å paints a different picture. These are shown in fig. 2.17 with the predicted fluxes for the exponential density model overlaid. The

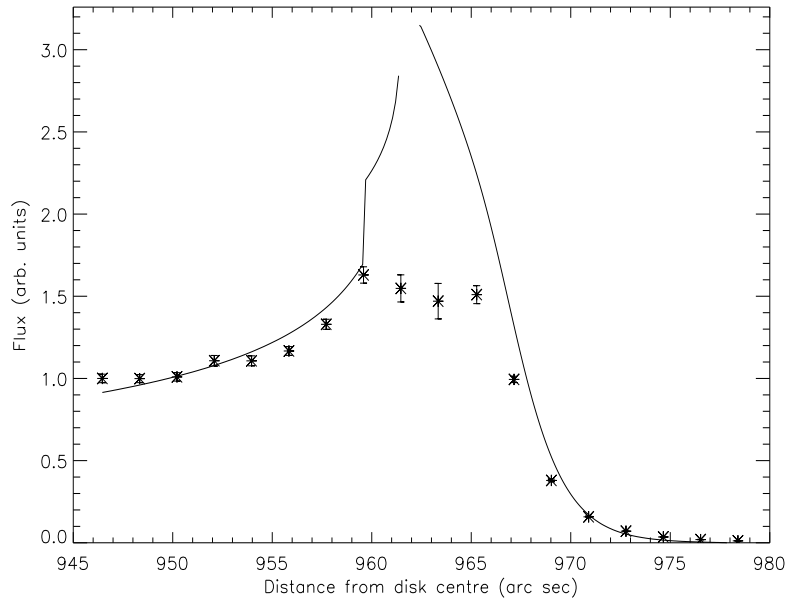


Figure 2.17: Observed fluxes for the C III $2s2p^3P_2 - 2p^2^3P_2$ line (1175.711 Å) line with model fluxes for the exponential density model (model 3) overlaid. The latter were calculated via eq. 2.43 and were scaled to match the observed points at 950.212 arc sec.

model fluxes were calculated using

$$I \sim \tau_0 \bar{g} \{ \tau_0 \} \quad (2.43)$$

Eq. 2.43 follows immediately from eq. 2.15 in the constant density case since $(N_u \Delta x) / \tau_0 = \text{const}$. It will be shown in chapter 3 that this also holds for the variable density case. It can be seen from fig. 2.17 that the model deviates markedly from the observed fluxes at the limb. This implies an overestimate in column density in the vicinity of the limb whereas fit to the ratios (fig. 2.16b) suggest that the model column densities are accurate in this region. In contrast, the fit to the fluxes at heights above ~ 970 arc sec is good whereas the fit to the ratios at these heights implies again an overestimation of column density.

Evidently there is a breakdown in the assumptions mentioned above in these regions. This can also be seen in table 2.1 where there are no optical depths extracted at heights 958.06 and 959.94 arc sec.

The good comparison to the ratios and fluxes on disk and in regions beyond the limb inspires confidence in the techniques but the real implications of making the assumptions listed above are unclear and consequently such techniques have so far only been considered as a useful approximation. In the subsequent chapters each of the assumptions listed will be considered and the discrepancies in the model will be addressed.